THE ASTRONOMICAL JOURNAL VOLUME 100, NUMBER 3 SEPTEMBER 1990

HIGH-VELOCITY MOLECULAR GAS ASSOCIATED WITH COLD *IRAS* SOURCES

BRUCE A. WILKING AND JAMES H. BLACKWELL
Department of Physics, University of Missouri-St. Louis, 8001 Natural Bridge Road, St. Louis, Missouri 63121

LEE G. MUNDY
Astronomy Program, University of Maryland, College Park, Maryland 20742
Received 16 April 1990

ABSTRACT

Maps are presented in the $J=2$–1 transition of CO for five molecular outflows associated with deeply embedded far-infrared sources. All of the outflows display lobes of both red- and blue-shifted gas with full velocity extents ranging from 37 to 63 km s^{-1}. At least two of the outflows are bipolar but neither is well-collimated. High-velocity ^{13}CO emission is detected in all sources. The data are used to estimate the optical depths, excitation temperatures, masses, momentum supply rates, and energy supply rates for the outflows. A comparison between the properties of *IRAS*-selected and optically selected molecular outflows is made. We find that the *IRAS*-selected outflows have significantly greater velocity extents and masses, and hence greater momenta and energies, than their optically selected counterparts when outflows with driving sources of similar luminosities are compared. However, the lobe sizes and dynamical lifetimes of the outflows do not show significant variation between these two samples. The results of this comparison can be understood in the context of a simple model for molecular outflows where local conditions determine the outflow size and the molecular gas decelerates and/or the wind breaks out of the cloud as the outflow evolves.

I. INTRODUCTION

Energetic mass loss occurs in association with an early, embedded phase of pre-main-sequence evolution when young objects are both intrinsically cool and heavily obscured by dust (Bally and Lada 1983; Berrilli *et al.* 1989; Margulis, Lada, and Young 1989). As a result, the bulk of their luminosity is radiated at far-infrared wavelengths. It is therefore not surprising that searches for molecular outflows toward flux-limited samples of *IRAS* sources have been very successful. Success ratios of 50% or greater have been reported from CO surveys of *IRAS* sources with steeply rising spectra from 12 to 100 μm (Casoli *et al.* 1986; Parker *et al.* 1988) and with $S_\nu(100\ \mu\mathrm{m}) > 400$ Jy (Snell *et al.* 1988; Snell, Dickman, and Huang 1990). Most recently, a CO survey of 50 cold *IRAS* sources with $S_\nu(100\ \mu\mathrm{m}) > S_\nu(60\ \mu\mathrm{m}) \geqslant 100$ Jy revealed 25 sources of high-velocity molecular gas with full velocity extents > 20 km s^{-1} (Wilking *et al.* 1989). A number of these are associated with well-studied bipolar molecular outflows such as L1551 IRS5 (e.g., Levreault 1988a), Mon R2 (Bally and Lada 1983), GGD12-15 (Rodriguez *et al.* 1982), IRAS 16293 − 2422 (Walker *et al.* 1988), S140 IR, and Cep A (e.g., Levreault 1988a).

In this paper, we present maps in the $J=2$–1 transition of CO of the high-velocity molecular gas toward five of the cold *IRAS* sources from the Wilking *et al.* (1989) survey (hereafter referred to as Paper I). Underscoring their deeply embedded nature is the fact that all of the sources are invisible and associated with dense concentrations of dust and gas ranging in size from < 0.015 to < 0.3 pc and containing 3–270 $\mathscr{M}_\odot$ (see Table I, Paper I). The high-velocity gas is found to arise in molecular outflows centered on the far-infrared sources with full velocity extents of 37–63 km s^{-1}. All of the outflows display both red- and blue-shifted gas and at least two are bipolar. Combining these data with ^{13}CO spectra at selected points within the outflows, we derive the mass, momentum supply rate, and energy supply rate for each outflow in the limits of optically thin and thick CO emission. Our data suggests the optically thick estimates are appropriate in most cases. Since the initial CO survey in Paper I, high-velocity gas has been fully mapped in 18 of these 25 prospective outflow sources. We will briefly discuss the collective outflow properties of these sources and compare them to a sample of optically selected molecular outflows.

II. OBSERVATIONS AND ANALYSIS

The $J=2$–1 rotational transitions of ^{12}CO (230.538 GHz) and ^{13}CO (220.399 GHz) were observed toward five cold *IRAS* sources; their positions, distances, and far-infrared luminosities are given in Table I. Observations were made with the NRAO* 12 m telescope located at Kitt Peak, Arizona during the period 25–29 March 1988. Spectra were obtained using a 128 channel filterbank with 500 kHz resolution, yielding a velocity resolution and coverage at 230 GHz of 0.65 and 83 km s^{-1}, respectively. The main beam width (FWHM) for the observations was 28″ and the forward beam efficiency, η_{FSS}, was 0.75 (Jewell 1988). Where conversions to T_R were necessary, the main beam efficiency, 0.50, was used as the source coupling efficiency, η_c (Kutner and Ulich 1981). Typical system temperatures during the observations, corrected for η_{FSS}, were 1500 K at 230 GHz and 1200 K at 220 GHz. Telescope pointing was checked periodically on Jupiter and Saturn; errors were usually found to be less than 5″. Observations of the standard sources Orion A, M17SW, and IRC + 10216 indicate uncertainties in absolute calibration of ~10%.

The primary goal of these observations was to map the

*The National Radio Astronomy Observatory is operated by Associated Universities, Inc., under contract with the National Science Foundation.

TABLE I. Properties of the cold *IRAS* sources.

IRAS Sources	R.A. (1950)			DEC. (1950)			Assoc.	Dist. (kpc)	L(7-135μm) ($L_\odot$)	θ (pc)	M_c ($M_\odot$)
05338-0624	5^h	33^m	$52\overset{s}{.}7$	-06°	24′	02″	L1641-N	0.45	120	<0.015	4.3
05375-0731	5	37	31.7	-07	31	59	L1641-S	0.45	<80	<0.026	3.2
18265-1517	18	26	32.9	-15	17	51	L379	2.0	<6000	0.13	270.
20126+4104	20	12	41.0	+41	04	20	Cygnus-X	1.7	<10000	<0.29	47.
21391+5802	21	39	10.3	+58	02	29	ICI396	0.75	260	<0.025	6.9

^{12}CO (hereafter referred to as CO) emission from the molecular outflows. Integration times were selected to obtain an rms noise in each spectrum of $\leqslant 100$ mK at 230 GHz and 50–80 mK at 220 GHz. Maps were made in CO with 40″ spacing to define the region with integrated high-velocity CO emission of $T_R^* > 2$ K km s^{-1}. Around positions of peak high-velocity emission, spectra were obtained with 20″ spacing. ^{13}CO spectra were always obtained at the positions of peak high-velocity emission and often at additional points within the outflow.

In our analysis, each outflow is characterized by the full velocity width, size, dynamical lifetime, and total mass. We define the full velocity width $\Delta v_{\max}$ as the maximum extent of the CO emission above the 100 mK level at any position in the map. A characteristic size for each outflow was estimated using the area defined by the lowest closed contours of integrated CO wing intensity common to both red- and blue-shifted gas. The major and minor axes of this total outflow area were measured and deconvolved assuming a Gaussian source and beam to yield the parameters $D_{\max}$ and $D_{\min}$. Dynamical timescales for the outflow were estimated in the standard manner as the ratio $D_{\max}/\Delta v_{\max}$ (e.g., Bally and Lada 1983).

Lower and upper limits for the outflow masses in each lobe were obtained under the assumption of optically thin and thick emission following the procedure described by Levreault (1988a). The first step in deriving masses involves integrating the high-velocity emission over the appropriate velocity interval. As is always the case, the inner boundary of the high-velocity component is difficult to define exactly. We identify this inner boundary as the velocity in the CO spectrum where the emission is dominated by the non-Gaussian wing component; as a result, low-velocity outflow gas in the CO line core is systematically neglected. In two sources, a velocity shift in the ambient cloud was observed across the outflow and the integration limits were adjusted accordingly. The next step requires estimating the optical depth and excitation temperature of the high-velocity gas. Average CO optical depths in red and blue lobes were calculated using the ratio of CO to ^{13}CO emission integrated over the portion of the CO high-velocity interval with detectable ^{13}CO emission. In the event that no ^{13}CO emission was detected outside of the CO line core, upper limits to the optical depths were obtained using the inner limit channels and the rms noise level of the ^{13}CO spectrum. A common surface filling factor and excitation temperature were assumed for both species. Excitation temperatures for the gas were estimated assuming that the surface filling factor of the lowest velocity outflow gas was unity; in this case, T_R in the lowest velocity channels, corrected for the Rayleigh–Jeans approximation, cosmic background radiation, and optical depth, directly yield values for T_{ex}. When this procedure resulted in a T_{ex} below 15 K, 15 K was assumed. The optically thick mass estimates assume that the optical depths calculated at the peak wing positions are constant over the outflow; this assumption appears to be valid for the IRAS 05338 − 0624 and 20126 + 4104 outflows where the optical depth could be estimated at several positions.

III. RESULTS

Spectra of the CO and ^{13}CO emission toward the positions of peak high-velocity emission in the five cold *IRAS* sources are shown in Figs. 1(a)–1(g). The integration limits for the high-velocity gas are shown as two sets of vertical lines. The full velocity widths of the outflows, given in Table II, vary from 37 to 63 km s^{-1}. As shown in Fig. 1 by the dashed line insets, all of the ^{13}CO spectra exhibit high-velocity emission; however, this emission often lies within the core of the broader CO line. The average CO optical depths, estimated from the spectra presented in Fig. 1, are given in Table II. There is good evidence that the CO emission from the peak wing positions in most of the outflows is optically thick in the (2–1) transition.

Maps of the integrated high-velocity CO emission are shown in Figs. 2(a)–2(e). The blue-shifted emission is traced by the dashed contours and the red-shifted emission by the solid contours; the bold cross in each map marks the *IRAS* source position. All sources display both red- and blue-shifted high-velocity gas which is clearly associated with the *IRAS* source. The major and minor axes of each outflow in parsecs are given in Table II. In the cases of IRAS 05338 − 0624 and IRAS 20126 + 4104 [Figs. 2(a) and 2(d)], the outflows are clearly bipolar but neither is highly collimated, i.e., the ratio of the major to minor outflow axis is < 2. While there is no clear separation of the peak red- and blue-shifted high-velocity gas toward *IRAS* 21391 + 5802, there are positions where one lobe dominates suggesting an underlying bipolar geometry.

Further outflow parameters, derivable from the data with more extensive assumptions are given in Table III. Estimates for the dynamical lifetimes of the outflows range from 1–3×10^4 yr and are typical of molecular outflows (Lada 1985; Levreault 1988a). Excitation temperatures could be derived for two sources and vary from 20–27 K. Outflow masses, estimated in the limit of optically thin and optically thick

TABLE II. Observed outflow parameters.

IRAS Source	Δv_{max} (km s^{-1})	D_{max} (pc)	D_{min} (pc)	D_{max}/D_{min}	$\bar{\tau}_r$	$\bar{\tau}_b$
05338-0624	44.8	0.46	0.30	1.5	3.1	6.9
05375-0731	36.7	>0.37	0.17	>2.0	<3.4[a]	<3.1[a]
18265-1517	48.8	1.63	0.95	1.7	5.9[b]	5.2[b]
20126+4104	63.1	1.35	0.81	1.7	6.5	10.5
21391+5802	42.9	0.61	0.25	2.4	<1.5[a]	<1.0[a]

Notes to TABLE II

[a] Upper limit to ^{12}CO optical depth derived for the inner limit channel using the ^{12}CO T_R^* and the rms noise level of the ^{13}CO spectrum.

[b] ^{13}CO data used to derive optical depth has low signal-to-noise ratio.

high-velocity gas, were used to compute momentum and energy supply rates using a velocity $V = \Delta v_{max}/2$. Both quantities scale roughly with the far-infrared luminosity of the embedded *IRAS* source. As is usually the case for molecular outflows, the mechanical luminosity is only a fraction (0.1%–8%) of the total radiant energy of the central object.

a) IRAS 05338−0624

This molecular outflow in Lynds 1641-North has been mapped in CO(1–0) by Fukui *et al.* (1986, 1988). In general, the distribution of high velocity gas in their 17″ resolution map resembles that in our (2–1) map at the 9 K km s^{-1} level and above. However the secondary peak in the western region of the red-shifted lobe, which is nearly comparable in strength to the primary peak in the (1–0) map, is only half the peak strength in (2–1). In addition, we observe red-shifted high-velocity gas over a larger area compared to the Fukui *et al.* (1–0) map [e.g., Fig. 2(a)]. In a (2–1) map with 1.2′ resolution obtained with the University of Texas Millimeter-Wave Observatory (MWO), low-level emission in the red-shifted lobe extends at least 5′ south of the *IRAS* position. The greater extent of the outflow in (2–1) is due to the fact that we have mapped the outflow down to a lower level (2 K km s^{-1} vs 9 K km s^{-1}) and that, toward the peak wing positions, the optical depth in the (2–1) transition is greater than that in (1–0) as reflected by the greater full velocity extent of the outflow (45 km s^{-1} vs 28 km s^{-1}). As a result, our estimates for the mass, momentum, and mechanical luminosity of the outflow are correspondingly greater than those of Fukui *et al.*

b) IRAS 05375−0731

In addition to the weak molecular outflow shown in Fig. 2(b), this far-infrared source is associated with an H_2O maser and a 6 cm continuum source (Wouterloot and Walmsley 1986; Morgan, Snell, and Strom 1990). The outflow has been mapped in CO(J = 1–0) by Morgan (1989) with 45″ resolution. He observes a weak lobe of red-shifted gas toward the *IRAS* source and a distinct blue-shifted lobe of comparable strength 1′ west and 30″ south. Our higher resolution CO(J = 2–1) map, while covering about the same area, does not indicate a bipolar geometry. Our map shows that the peak of the blue- and red-shifted gas are coincident with the *IRAS* source to within our resolution and that the blue-shifted lobe is about twice the strength of the red-shifted lobe. Since our map is not completely sampled along the outflow axis, we cannot rule out the presence of a second blue-shifted component in the vicinity of that observed by Morgan.

c) IRAS 18625−1517

Our CO(2–1) map of this outflow in the Lynds 379 cloud shows that the intensities of both the red- and blue-shifted high-velocity gas are a maximum at the *IRAS* source position [Fig. 2(c)]. We do not see the bipolar structure which is evident in the 80″ resolution map in CO(2–1) presented by Hilton *et al.* (1986). Although not presented here, 1.2′ resolution observations with the MWO in CO(2–1) display no evidence for the maximum in the blue-shifted lobe intensity shown by their map 3′ south of the *IRAS* source. Perhaps the discrepancy arises from their velocity coverage of 20 km s^{-1} which is much less than the full velocity extent of 49 km s^{-1} for the high-velocity gas measured by our observations. The outflow mass and mechanical luminosity which we derive are larger than those determined by Hilton *et al.*, primarily due to our greater estimate for the distance to the source (2000 vs 200 pc, Paper I). In agreement with their observations, we observe the peak emission from the ambient cloud at the *IRAS* source position and a northwest–southeast velocity gradient in the ambient cloud.

d) IRAS 20126+4104

This previously unobserved outflow, situated in a dark globule in the Cygnus-X region, displays the highest velocity gas of the objects in our study. The outflow encompasses most of the molecular cloud core (radius = 100″) in which it resides. ^{13}CO spectra were obtained at six positions within

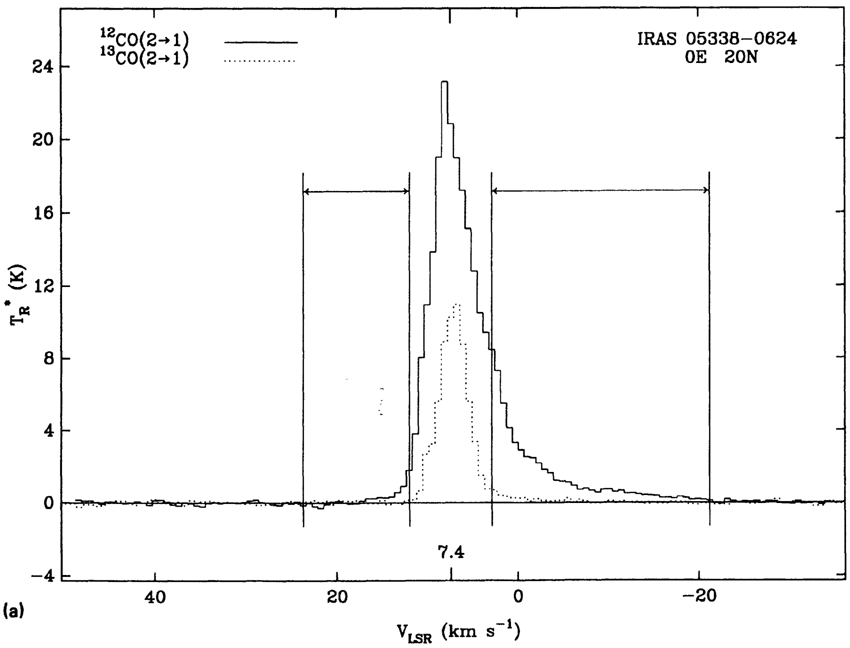

(a)

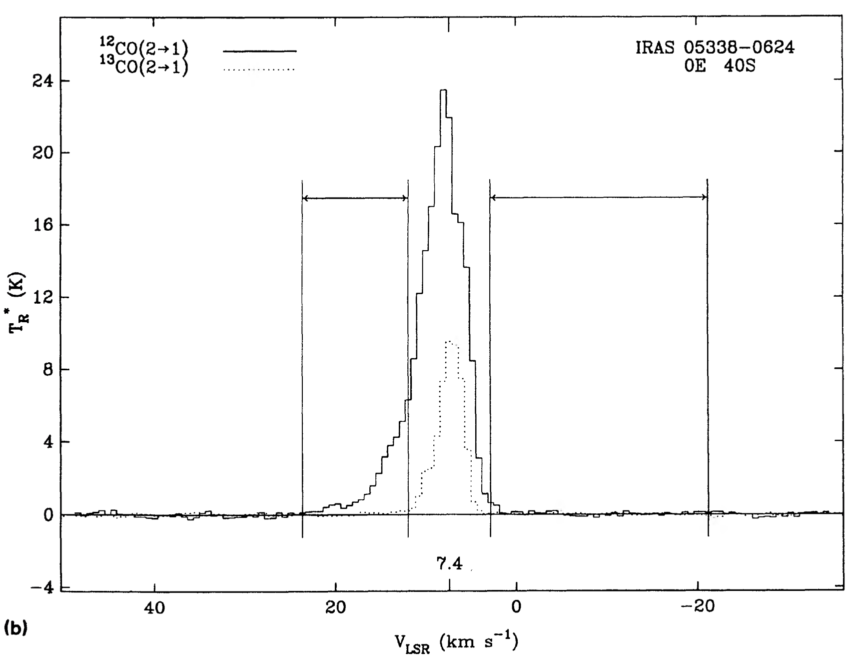

(b)

FIG. 1. ^{12}CO($J = 2$–1) and ^{13}CO($J = 2$–1) spectra toward the positions of maximum integrated wing intensity for the five outflow sources. Each pair of spectra is in units of T_R^* and drawn to the same scale. The offset of the spectra in arcseconds from the *IRAS* source position is given in the top right-hand corner. Integration limits are indicated by the two sets of vertical bars. The velocity of the ambient cloud is labeled below the spectra. (a) The position of peak blue-shifted emission associated with IRAS 05338 − 0624. (b) The position of peak red-shifted emission associated with IRAS 05338 − 0624. (c) Peak red- and blue-shifted emission coincident with IRAS 05375 − 0731. (d) Peak red- and blue-shifted emission coincident with IRAS 18265 − 1517. (e) The position of peak blue-shifted emission associated with IRAS 20126 + 4104. (f) The position of peak red-shifted emission associated with IRAS 20126 + 4104. (g) Peak red- and blue-shifted emission coincident with IRAS 21391 + 5802.

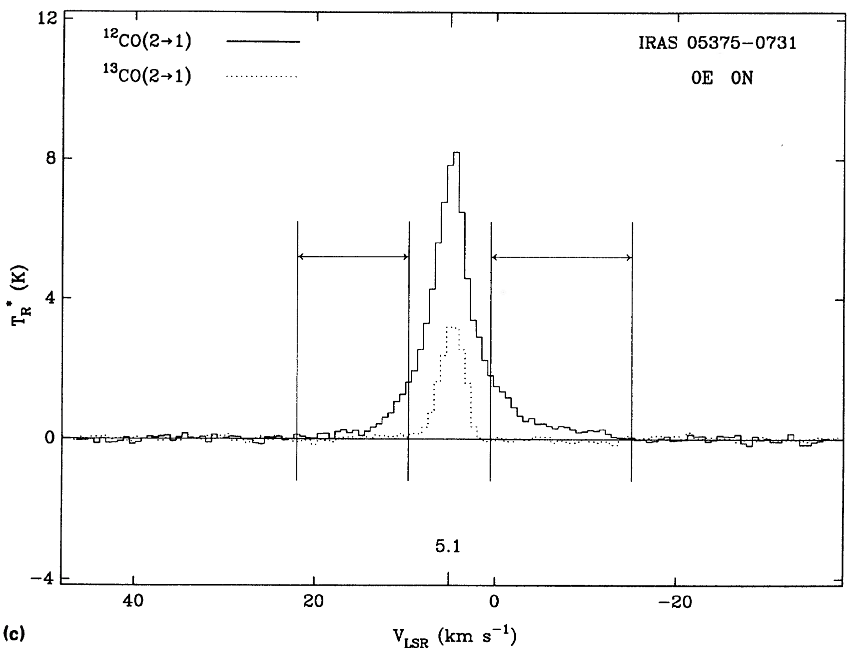

(c)

FIG. 1. (continued)

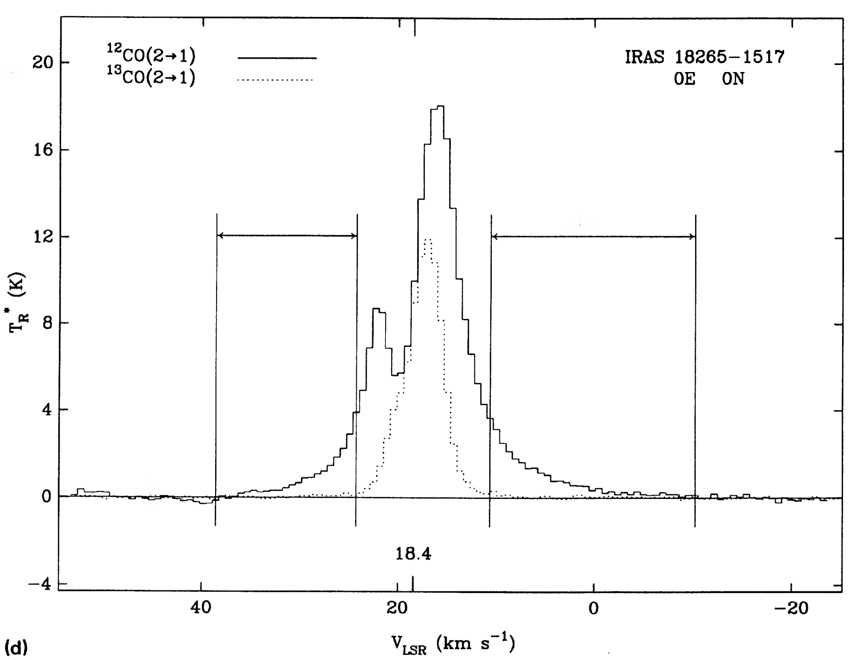

(d)

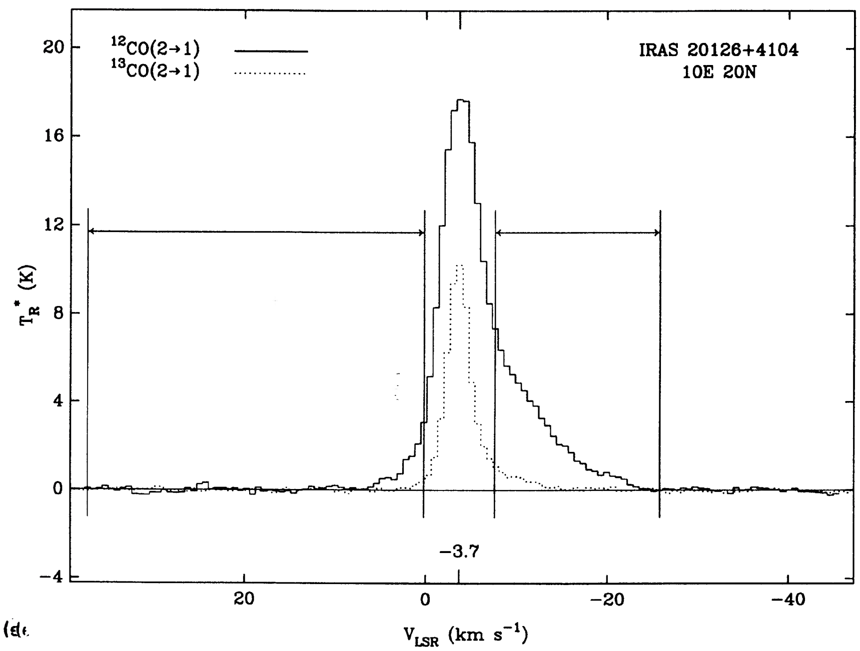

(e)

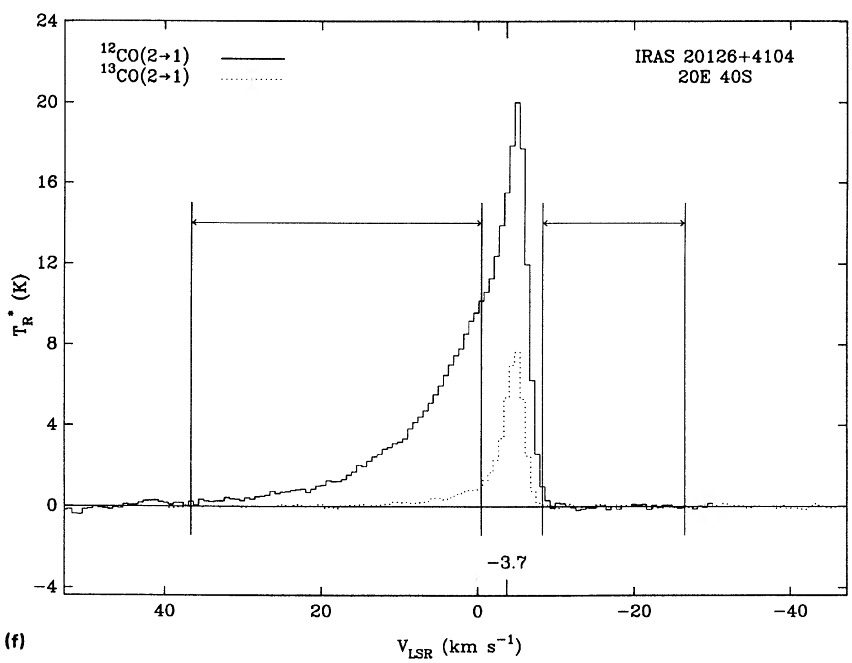

(f)

FIG. 1. (continued)

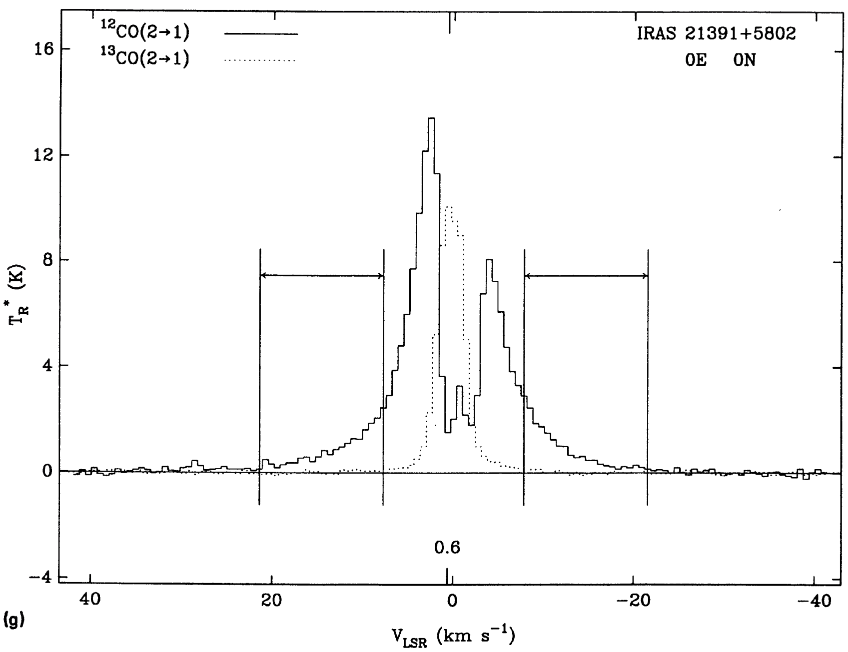

(g)

FIG. 1. (continued)

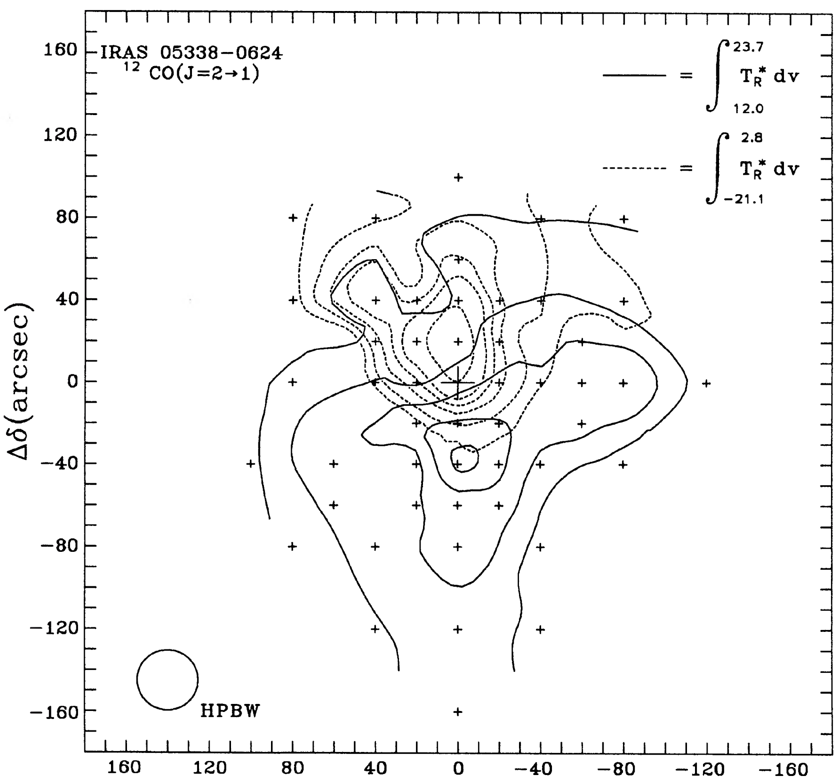

(a)

FIG. 2. Maps of CO integrated intensity for the five outflow sources. The integration limits in velocity for the red- and blue-shifted gas are indicated at top right in units of km s^{-1}. The lowest contour level and contour intervals are identical for both the red- and blue-shifted gas in a given map. Dashed contours represent the blue-shifted gas and solid contours the red-shifted gas. The 28″ HPBW is shown in the lower left corner. The (0,0) position of each map, marked by a large cross, is the position of the *IRAS* source. Small crosses mark the positions observed in CO. (a) The bipolar outflow associated with IRAS 05338 − 0624. The contour levels are 2, 5, 10, 15, 20, 30, and 40 K km s^{-1}. (b) The outflow associated with IRAS 05375 − 0731. The contour levels are 2, 4, 6, 8, and 10 K km s^{-1}. (c) The outflow associated with IRAS 18265 − 1517. The contour levels are 2, 5, 10, and 15 K km s^{-1}. (d) The bipolar outflow associated with IRAS 20126 + 4104. The contour levels are 2, 5, 10, 20, 30, 50, 75, and 100 K km s^{-1}. (e) The outflow associated with IRAS 21391 + 5802. The contour levels are 2, 4, 6, 8, and 10 K km s^{-1}.

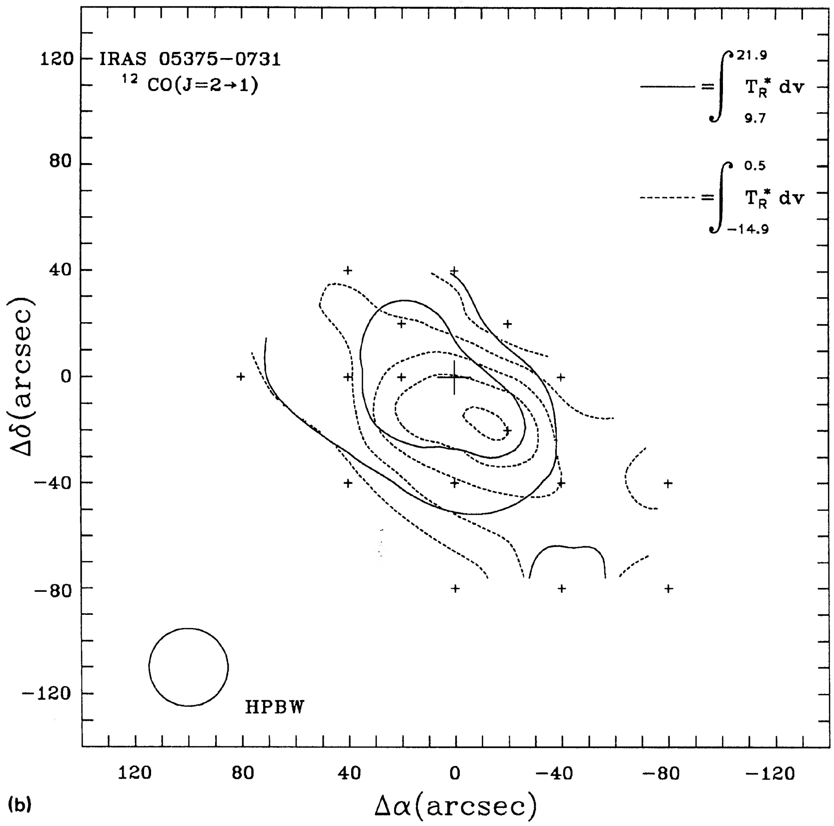

(b)

FIG. 2. (continued)

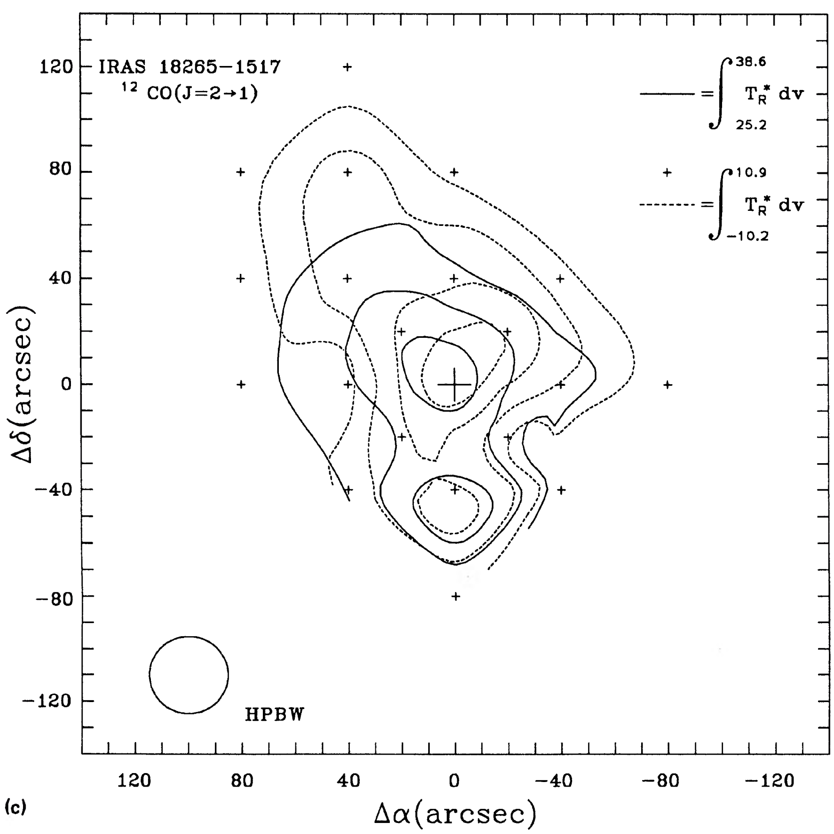

(c)

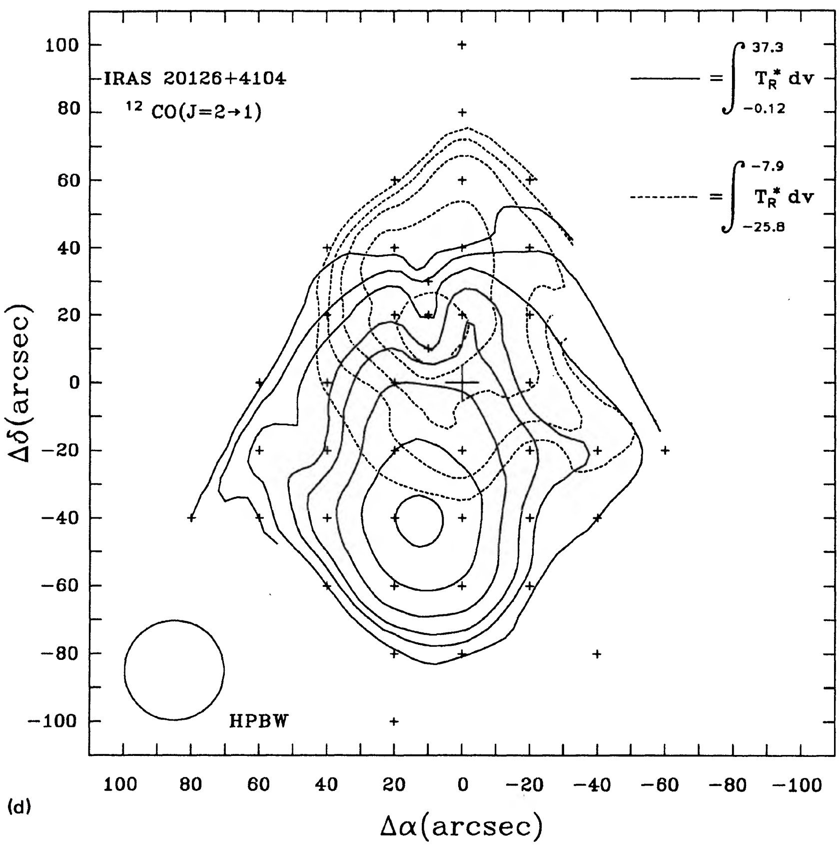

(d)

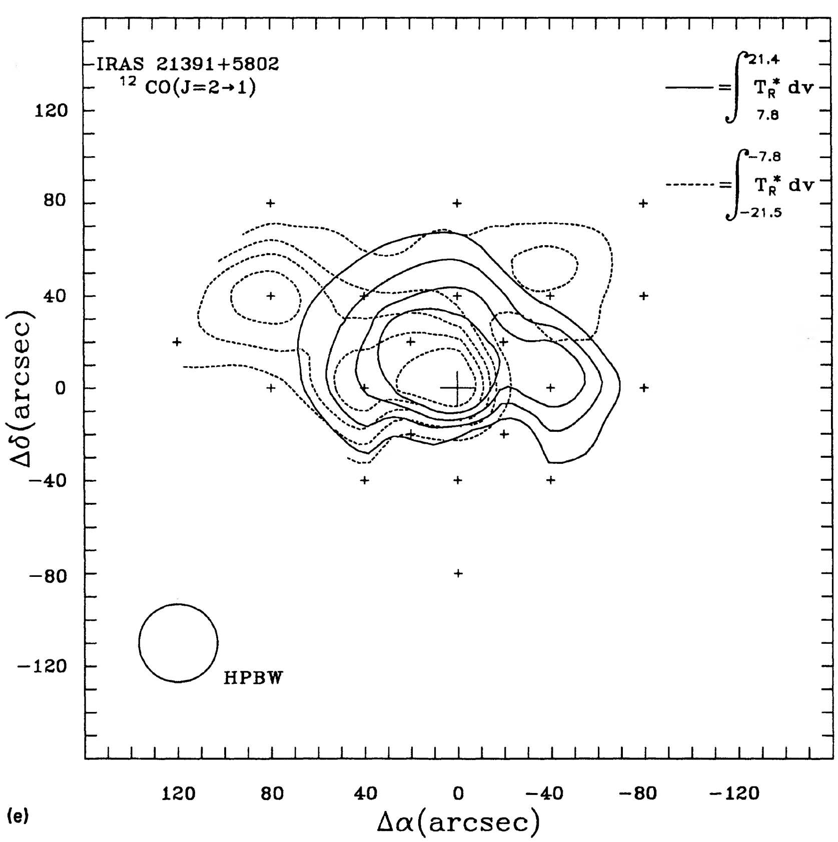

(e)

FIG. 2. (continued)

TABLE III. Derived outflow parameters.

IRAS Source	$T_{ex,r}$ (K)	$T_{ex,b}$ (K)	τ_{dyn} (yr)	$M_{thin,r}$ ($M_\odot$)	$M_{thin,b}$ ($M_\odot$)	$M_{thick,r}$ ($M_\odot$)	$M_{thick,b}$ ($M_\odot$)	$\dot{M}_T V^b$ ($M_\odot$ km/s/yr)	$\frac{1}{2}\dot{M}_T V^{2b}$ ($L_\odot$)
05338-0624	20	23	9.9×10^3	0.29	0.18	0.94	1.24	1.0-4.9 $\times10^{-3}$	2.0-9.1
05375-0731	15[a]	15[a]	$>9.9\times10^3$	0.033	0.081	0.12	0.26	<2.1-7.0 $\times10^{-4}$	<0.32-1.1
18265-1517	15[a]	15[a]	3.3×10^4	1.4	2.5	8.3	13	0.3-1.6 $\times10^{-2}$	5.8-32
20126+4104	27	21	2.1×10^4	7.2	1.9	47	20	0.1-1.0 $\times10^{-1}$	36-260
21391+5802	15[a]	15[a]	1.4×10^4	0.19	0.24	0.37	0.38	0.7-1.1 $\times10^{-3}$	1.2-2.0

Notes to TABLE III

[a] A value of 15 K is assumed.
[b] Range of values represent those for optically thin and optically thick CO emission.

the outflow and indicate that emission from the high-velocity gas is optically thick throughout. As in the case of 18265 − 1517, the CO emission from the ambient cloud reaches a maximum at the *IRAS* source position. A shift of 1.6 km s^{-1} in the velocity of the ambient cloud was observed across the outflow in roughly a north–south direction. A $\lambda = 2.2$ μm survey of a one square arcmin area centered on the *IRAS* source position has revealed a heavily reddened object 2″ east and 5″ south of map center (Wilking and Walker, unpublished data). The infrared magnitudes at 2.2, 4.8, 10.2, and 20 μm are measured to be 9.9, 6.2, 4.5, and − 1.5 within a 6″ (2.2 μm only) or 8″ beam. These magnitudes are consistent with the *IRAS* flux densities and suggest the presence of a strong silicate absorption.

e) IRAS 21391+5802

The distribution of high-velocity gas determined from our observations agrees well with the CO(1–0) observations obtained by Sugitani *et al.* (1989) with 17″ resolution. Our data suggests that the orientation of the outflow axis is roughly at a position angle of 75°. Like the IRAS 20126 + 4104 outflow, the high velocity molecular gas involves a significant fraction of the globule in which the *IRAS* source is embedded. The location of the IC 1396-E globule at the edge of the Cep OB2 giant H II region raises the question of whether the formation of this embedded source could have been triggered by ionization-shock fronts from the H II region. A comparison of the dynamical lifetime of the outflow, the timescale for propagation of these fronts through the globule, and the age of the H II region has led Sugitani *et al.* to suggest that such a scenario is possible. As a further manifestation of the outflow, Gyulbudaghian, Rodriguez, and Curiel (1990) have discovered H_2O masers at both red- and blue-shifted velocities within a 90″ beam centered on the *IRAS* source position.

IV. IMPLICATIONS FOR THE EVOLUTION OF MOLECULAR OUTFLOWS

With the inclusion of the five sources in this study, high-velocity molecular gas has been fully mapped for 18 of the 25 cold far-infrared sources from Paper I which were suspected to have outflows. Among these 18 sources, 17 appear to be associated with molecular outflows. All of the outflows, except for IRAS 06384 + 0932 (NGC 2264-IR), show both blue- and red-shifted high-velocity gas and 12 exhibit bipolar morphologies. The association of IRAS 06308 + 0402 with an outflow is less certain because of the complex velocity structure of the molecular gas (Snell, Dickman, and Huang 1990). In addition, this *IRAS* source is coincident with a well-resolved, dust-obscured H II region which may dominate the far-infrared emission but could be unrelated to outflow activity (Paper I).

In Table IV, we have compiled data for 17 of the 18 regions of high-velocity gas associated with cold far-infrared sources studied in Paper I. CO(J = 2–1) data was used when available. We have excluded the IRAS 05373 + 2349 outflow (Casoli *et al.* 1986) due to lack of information. The data consist of the fundamental observable quantities of the outflows (full velocity extents, maximum radii, and masses) and the standard derived outflow parameters (dynamical lifetimes, momenta, and energies). Outflow mass estimates in Table IV ignore the contribution from low-velocity gas in the line core. Dynamical lifetimes were computed to conform with the definition presented in Sec. II. The sources are listed in order of increasing far-infrared luminosity of the associated source. Despite scatter, the data in Table IV [also shown in Fig. 3(c)] indicate a weak but significant dependence of the outflow mass with source luminosity. A least-squares fit to the data yields $\mathcal{M} \propto L^{0.5\pm0.3}$. No significant correlation is seen between outflow size or velocity extent and source luminosity.

Since our *IRAS*-selected sample is expected to represent objects in an early phase of pre-main-sequence evolution, we can look for evolutionary effects in the outflow parameters through a comparison with a sample of optically selected, and therefore presumably older, molecular outflows. For this comparison, we have considered the properties of 16 outflows associated with visible pre-main-sequence stars investigated by Levreault in the CO(2–1) transition (1988a,b). The parameters for these optically selected outflows were reanalyzed in the manner described for the objects in this study. Ten of the outflows show only one outflow lobe (six with blue-shifted lobes and four with red-shifted

TABLE IV. Properties of the cold source outflows.

IRAS Source	Association	Log (L_{FIR})	CO	Ref.	Δv_{max} (km s^{-1})	Mass ($M_\odot$)	R_{max} (pc)	τ_{dyn} (yr)	Momentum ($M_\odot$ km s^{-1})	Energy (ergs)
16293-2422	L1689N	1.4	2-1	(1)	32.0	0.8	0.13	8.0×10^3	13	2.0×10^{45}
04287+1801	L1551-IRS5	1.4	2-1	(2)	38.6	0.55	0.55	2.8×10^4	11	2.0×10^{45}
05375-0731	L1641-S	1.9	2-1	(3)	36.8	0.38	0.18	9.9×10^3	7	1.3×10^{45}
05338-0624	L1641-N	2.1	2-1	(3)	44.8	2.2	0.23	9.9×10^3	49	1.1×10^{46}
05380-0728	R50	2.2	1-0	(4)	16.0	2.5	0.61	7.5×10^4	20	1.6×10^{45}
21391+5802	IC1396	2.4	2-1	(3)	42.9	0.75	0.30	1.4×10^4	16	3.5×10^{45}
06382+0939	NGC2264	2.6	1-0	(5)	34.5	16	1.20	6.9×10^4	280	4.8×10^{46}
06384+0932	NGC2264-IR	3.4	1-0	(5)	21.4	1.6	0.24	1.1×10^4	34	7.3×10^{45}
06308+0402		3.6	1-0	(6)	12.0	7	0.86	1.4×10^5	42	2.5×10^{47}
00494+5617	NGC281	3.7	1-0	(6)	20.0	11	1.30	1.3×10^5	110	1.1×10^{46}
18265-1517	L379	3.8	2-1	(3)	48.8	21	0.82	3.3×10^4	510	1.3×10^{47}
05358+3543	S235	3.8	1-0	(6)	25.0	16	1.00	8.5×10^4	200	2.5×10^{46}
06084-0611	GGD12-15	4.0	1-0	(7)	25.0	1	0.28	2.2×10^4	13	1.6×10^{45}
20126+4104		4.0	2-1	(3)	63.1	67	0.68	2.1×10^4	2100	6.7×10^{47}
22543+6145	Cep A	4.2	2-1	(2)	40.0	5	1.2	6.0×10^4	100	2.0×10^{46}
22176+6303	S140-IR	4.4	1-0	(8)	40.0	24	0.11	5.4×10^3	480	9.6×10^{46}
06053-0622	Mon R2	4.6	1-0	(9)	31.0	50	2.10	1.3×10^5	1775	1.2×10^{47}

References - (1) Walker *et al.* 1988, (2) Levreault 1988, (3) this study, (4) Reipurth and Bally 1986, (5) Margulis, Lada, and Snell 1988, (6) Snell, Dickman, and Huang 1990, (7) Rodriguez *et al.* 1982, (8) Snell *et al.* 1984, and (9) Bally and Lada 1983.

lobes), a significantly higher percentage of monopolar outflows than in the *IRAS*-selected sample. To reduce the bias in size and velocity introduced by single-lobed outflows, the comparison of the two samples was made in terms of the velocity extents and sizes of a single lobe. For two-lobed outflows, average quantities are given by $\Delta v_{max}/2$ and $R_{max} = D_{max}/2$.

Graphical comparisons of the half-velocity extents, average lobe sizes, and outflow masses for the two datasets are shown in Figs. 3(a), 3(b), and 3(c). There is clearly considerable scatter in the values in all three figures. This scatter is caused in part by uncertainties introduced by using a heterogeneous dataset for the *IRAS*-selected sample and uncertainties arising from the choice of inner velocity limits for the outflows in both datasets. The intrinsic variations in the orientation of the outflow axis with respect to the line-of-sight and in the molecular environment of individual outflows must also contribute to the scatter. For outflows with source luminosities between 10 and 1000 $L_\odot$, there is a marked tendency for the *IRAS*-selected sources to have greater outflow masses and half-velocity extents by factors of roughly 3 and 2, respectively. Similarly, momenta and energies of the *IRAS*-selected outflows are greater by factors of roughly 6 and 12. The lobe sizes show no statistically significant variation between the two samples. For sources luminosities below 10 $L_\odot$ or above 1000 $L_\odot$ the overlap of the two samples is insufficient to permit a reasonable comparison.

How do the results of this comparison match up with expectations? Adopting a simple picture for bipolar outflows, we presume that a very high-velocity wind of neutral and ionized gas emanates from the central source, providing a relatively constant supply of momentum and energy to the two outflow lobes. In response to the continuing input from the wind, high-velocity molecular gas (mainly material swept up by the expanding lobes) increases in spatial extent, mass, momentum, and energy with time. As the mass of swept-up material increases, however, the velocity in the outer parts of the outflow decreases. Eventually the lower velocity material begins to blend in with the ambient cloud, resulting in a loss of mass, momentum, and energy from the identifiable outflow. A loss of observable outflow mass can also occur if the wind manages to break out of the molecular cloud since it can no longer sweep up new material and the material already in the outflow is subject to dissociation by the interstellar radiation field. This simple scenario suggests that outflows in the *IRAS*-selected sample should generally exhibit smaller lobe sizes, greater velocity extents, and greater masses than those in the optically selected sample.

Hence, the relative youth of the *IRAS*-selected outflows appears to be reflected in their greater observed masses and velocities. The predominance of monopolar outflows in the optically selected sample (10 of 16), which is largely responsible for the mass difference between these two samples, suggests that the break-out of the wind from the molecular cloud may be an important effect in their evolution. However, the sizes of the lobes in *IRAS*-selected outflows are not smaller by a statistically significant amount than those in the optically selected sample. Perhaps this is an indication that local conditions, such as cloud density and geometry, may be more important in determining lobe size than outflow age. In

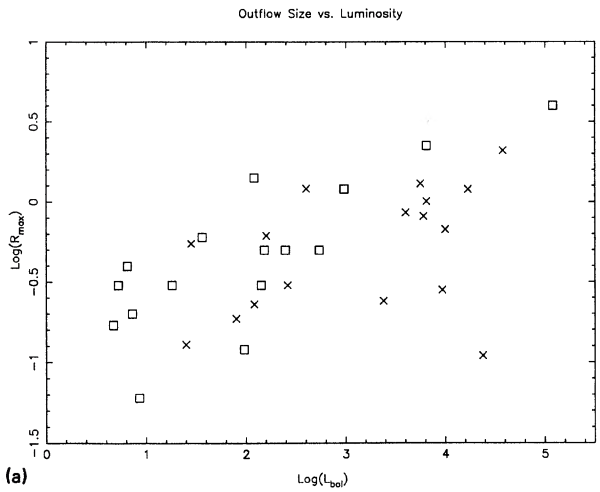

(a)

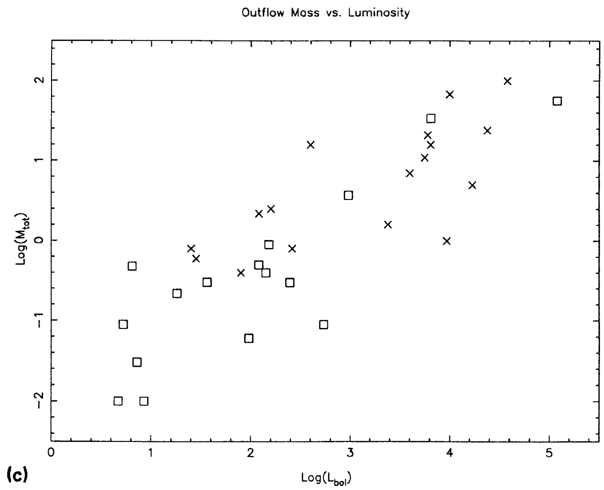

(c)

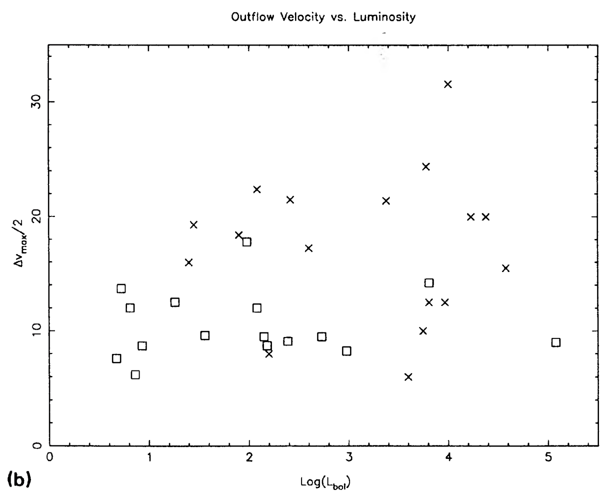

(b)

FIG. 3. Fundamental outflow parameters as a function of the bolometric luminosity of the driving source. Outflow parameters derived from *IRAS*-selected sources are represented by an $\times$ and those derived from optically selected sources are shown by a square. For the *IRAS* sources, it is assumed that the far-infrared luminosity is a good approximation of the bolometric luminosity. (a) A log–log plot of the outflow size ($R_{\max}$ in parsecs) vs luminosity (in $L_\odot$). (b) A plot of the outflow half-velocity extent ($\Delta v_{\max}/2$ in km s^{-1}) vs log(luminosity in $L_\odot$). (c) A log–log plot of the total outflow mass (in $\mathscr{M}_\odot$) vs luminosity (in $L_\odot$). For the combined sample, the outflow mass increases as $L^{0.71 \pm 0.14}$. This trend could be explained if the volume of the outflow lobes increases with source luminosity, predicting the outflow radius $R_{\max} \propto L^{0.24}$. Unfortunately, such a weak dependence of $R_{\max}$ with L cannot be observed given the noise of these data [Fig. 3(a)].

light of the small differences in outflow lobe sizes and only factor of 2 differences in velocity extents between the two comparison samples, it is not surprising that the dynamical lifetimes calculated for the two samples are not dramatically different. For central sources with luminosities between 10 and 1000 $L_\odot$, the harmonic mean of the dynamical lifetimes are 2×10^4 and 4×10^4 yr for the *IRAS*-selected and optically selected samples, respectively. However, this difference is not statistically significant since the scatter in these timescales within each sample spans roughly an order of magnitude. Therefore, the dynamical lifetime appears to be a poor measure of the absolute age of the outflow. Consideration of our simple outflow model, which allows for the deceleration of the high-velocity molecular gas or break-out of the wind from the cloud as the outflow evolves, suggests that the physical significance of the simple dynamical lifetime ($2R_{\max}/\Delta v_{\max}$) is difficult to ascertain in an evolved outflow. As larger samples of well-studied molecular outflows become available, it should become possible to make more detailed studies of evolutionary trends in the fundamental parameters observed for outflows.

We would like to thank Phil Jewell, Russ Levreault, and Charles Lada for helpful discussions on the reduction and interpretation of the data. We are grateful to John Howe and Chris Walker for assistance with the observations.

REFERENCES

Bally, J., and Lada, C. J. (1983). Astrophys. J. Lett. **265**, 824.

Berrilli, F., Ceccarelli, C., Liseau, R., Lorenzetti, D., Saraceno, P., and Spinoglio, L. (1989), Mon. Not. R. Astron. Soc. **203**, 367.

Casoli, F., Dupraz, C., Gerin, M., Combes, F., and Boulanger, F. (1986), Astron. Astrophys. **169**, 281.

Fukui, Y., Sugitani, K., Takaba, H., Iwata, T., Mizuno, A., Ogawa, H., and Kawabata, K. (1986). Astrophys. J. Lett. **311**, L85.

Fukui, Y., Takaba, H., Iwata, T., and Mizuno, A. (1988). Astrophys. J. Lett. **325**, L13.

Gyulbudaghian, A. L., Rodriguez, L. F., and Curiel, S. (1990). Preprint.

Hilton, J., White, G. J., Cronin, N. J., and Rainey, R. (1986). Astron. Astrophys. **154**, 274.

Jewell, P. R. (1988). NRAO 12 m Telescope Receiver and Calibration Status.

Kutner, M. L., and Ulich, B. L. (1981). Astron. J. **250**, 341.
Lada, C. J. (1985). Annu. Rev. Astron. Astophys. **23**, 267.
Levreault, R. M. (1988a). Astrophys. J. Suppl. **67**, 283.
Levreault, R. M. (1988b). Astrophys. J. **330**, 897.
Margulis, M., Lada, C: J., and Snell, R. L. (1988). Astrophys. J. **333**, 316.
Margulis, M., Lada, C. J., and Young, E. T. (1989). Astrophys. J. **345**, 906.
Morgan, J. (1989), Ph.D. thesis, University of Massachusetts.
Morgan, J., Snell, R. L., and Strom, K. M. (1990). Preprint.
Parker, N. D., Padman, R., Scott, P. F., and Hills, R. E. (1988). Mon. Not. R. Astron. Soc. **234**, 67P.
Reipurth, B. and Bally, J. (1986). Nature **320**, 326.
Rodriguez, L. F., Carral, P., Ho, P. T. P., and Moran, J. M. (1982). Astrophys. J. **260**, 635.
Snell, R. L., Dickman, R. L., and Huang, Y.-L. (1990). Astrophys. J. **352**, 139.
Snell, R. L., Huang, Y.-L., Dickman, R. L., and Claussen, M. J. (1988). Astrophys. J. **325**, 853.
Snell, R. L., Scoville, N. Z., Sanders, D. B., and Erickson, N. R. (1984). Astrophys. J. **284**, 176.
Sugitani, K., Fukui, Y., Mizuno, A., and Ohashi, N. (1989). Astrophys. J. Lett. **342**, L87.
Walker, C. K., Lada, C. J., Young, E. T., and Margulis, M. (1988). Astrophys. J. **332**, 335.
Wilking, B. A., Mundy, L. G., Blackwell, J. H., and Howe, J. E. (1989). Astrophys. J. **345**, 257 (Paper I).
Wouterloot, J. G. A., and Walmsley, C. M. (1986). Astron. Astrophys. **168**, 237.

THE ASTRONOMICAL JOURNAL

FOUNDED BY B. A. GOULD
1849

VOLUME 100 **September 1990 ~ No. 1616** NUMBER 3

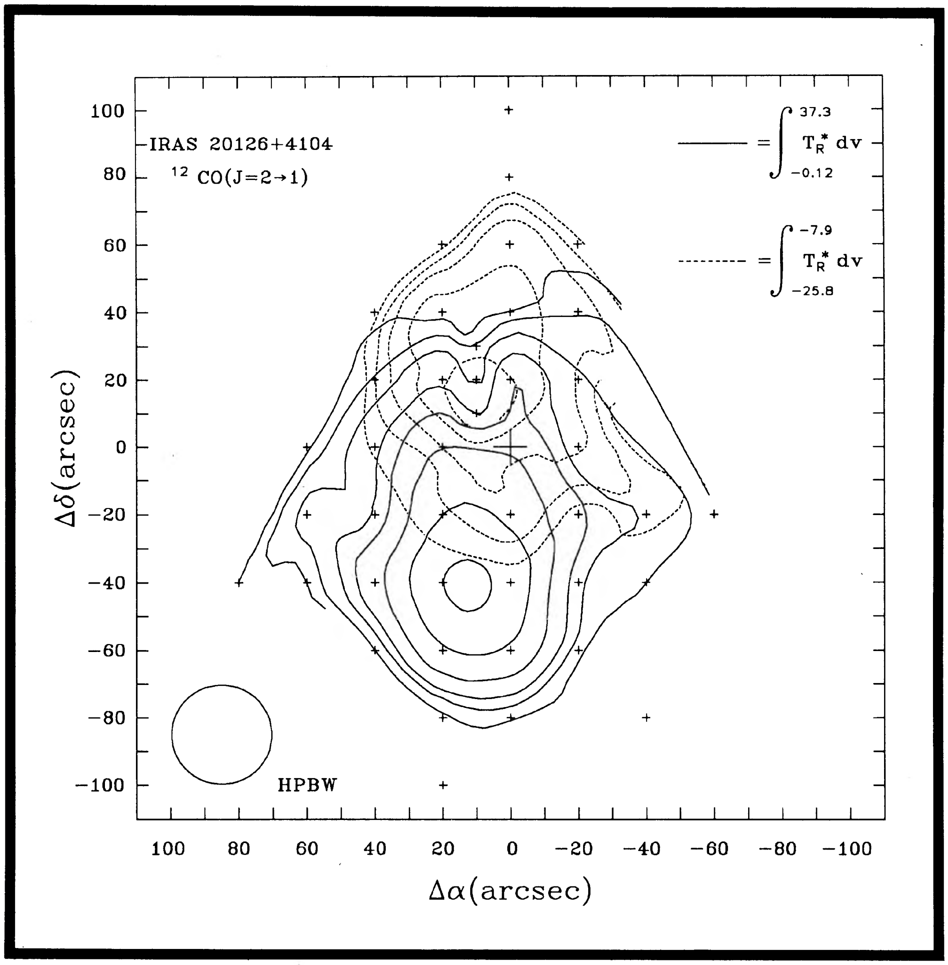

(See Page 758)

Published for the
AMERICAN ASTRONOMICAL SOCIETY
by the
AMERICAN INSTITUTE OF PHYSICS